Research Square

Preprints are preliminary reports that have not undergone peer review.
They should not be considered conclusive, used to inform clinical practice,
or referenced by the media as validated information.

Thermoring-driven allosteric gating coupling in TRPV2

Guangyu Wang

gary.wang10@gmail.com

University of California, Davis

Research Article

Keywords: allosteric gating coupling, digital biology, thermoring energetic structure, temperature threshold

Posted Date: November 5th, 2026

DOI: https://doi.org/10.21203/rs.3.rs-11614966/v1

License: This work is licensed under a Creative Commons Attribution 4.0 International License.
Read Full License

Additional Declarations: The authors declare no competing interests.

Abstract

Allosteric regulation of protein activity by chemical stimuli has been extensively investigated, whereas the effects of physical stimuli remain comparatively poorly understood. In this computational study, a highly sensitive thermoring energetic model was employed to analyze the three-dimensional structures of homotetrameric, thermosensitive transient receptor potential vanilloid 2 (TRPV2) channels following a species-specific residue swap near the central lower gate in rat and human TRPV2. In the rat TRPV2 triple mutant, the swap-induced symmetry breaking partially disrupted the interfacial swapping π bridges between the S4-S5 linker and S5' near the central lower gate. It also altered the location of the superficial weakest tertiary noncovalent bridge and shifted the corresponding melting threshold for heat activation. In contrast, the equivalent residue swap in human TRPV2 preserved C4-fold symmetry, the identity of the superficial weakest bridge and its corresponding melting threshold for heat activation, as well as the interfacial swapping π bridges. Notably, the residue swap in human TRPV2 simultaneously weakened the weakest and swapping bridges, thereby enhancing heat-evoked activity while lowering the heat-activation threshold. Taken together, these findings suggest that when the superficial weakest bridges function as putative heat sensors, C4-fold symmetry is essential for their allosteric gating coupling to the interfacial swapping π bridges. (202 words)

introduction

Allosteric regulation of protein activity through genetic or chemical perturbations has been extensively investigated, both experimentally and theoretically (1–13). In contrast, the mechanisms by which physical perturbations, such as heat or cold, regulate protein function have remained considerably less understood, particularly before the identification of the homotetrameric, thermosensitive transient receptor potential vanilloid 1 (TRPV1) channel was identified in 1997 (14).

The thermosensitive TRPV1-4 channels share a highly conserved structural motif, Y_nR/K_{n+14}, that forms interfacial swapping bridges between the S4-S5 linker and S5' near the central lower gate, thereby locking the channels in their closed state (15–22). These channels also exhibit distinct heat activation thresholds: 25–35 C for TRPV4, 32–49°C for TRPV3, 42°C for TRPV1 and 52°C for TRPV2 (14, 23–31). Recent thermoring energetic analyses of their cryo electron microscopy (cryo-EM) structures have identified a specific weakest tertiary noncovalent bridge in each of TRPV1, TRPV3 or TRPV4, whose melting threshold closely matches the corresponding heat-activation threshold. These findings suggest that the weakest bridge in each channel may serve as a putative heat sensor (19–22, 32).

Notably, in the closed state, these weakest bridges are located on the protein surface, spatially distant from the interfacial swapping Y_n-R'/K' $_{n+14}$ π bridges. Upon channel opening, the superficial weakest bridges are disrupted concomitantly with the breaking of swapping Y_n-R'/K' $_{n+14}$ π bridges (16, 21–22). Based on these structural and energetic relationships, the superficial weakest bridges have been proposed to allosterically couple with the interfacial swapping π bridges near the central lower gates, thereby mediating heat activation of TRPV1, TRPV3 and TRPV4 channels (21–22).

On the other hand, rat TRPV2 (rTRPV2) has at least three superficial weakest tertiary bridges with melting thresholds that match its relatively high heat-activation threshold of approximately 48–55°C (28–34). Because capturing the open state at such elevated temperatures remains challenging, it is still unknown which of these weakest bridges is allosterically coupled to the interfacial swapping π bridges. Given the reversible nature of signaling transduction between an allosteric regulatory site and a distant effect site (35), it is reasonable to expect that perturbations of the interfacial swapping π-bridges may reciprocally affect the superficial weakest bridges. Consistent with this possibility, disrupting the swapping Y575-K589’ bridge near the central lower gate by a phosphatidylcholine (PC) lipid is accompanied by the broken weakest E467-K545 bridge in the inactivated state of oxidized human TRPV3 (hTRPV3) (PDB ID: 8GKA) (36). Similarly, both the weakest P494/Y498-Y563 bridges and the swapping Y598-R612’ bridges are disconnected in an inactivated state of amphibian TRPV4 (16, 21, 37). Therefore, it is hypothesized that a genetic perturbation near the central lower gate of TRPV2 may provide a means of investigating the allosteric coupling between the superficial weakest tertiary bridges and the interfacial swapping π-bridges.

To test this hypothesis, three-dimensional cryo-EM structures of rTRPV2 and human TRPV2 (hTRPV2) containing species-specific residue swaps at the TRP/S6 interface were analyzed using a highly sensitive thermoring energetic model (38). The results revealed that the interfacial swap in the rTRPV2$_{STD}$ triple mutant induced symmetric break, accompanied by relocation of the superficial weakest bridge with a matched melting threshold and partial disruption of the interfacial swapping bridge between the S4-S5 linker and S5’in the C2-symmetric subunits. In contrast, the corresponding interfacial swap in the hTRPV2$_{HDN}$ triple mutant preserved C4-fold symmetry, the location of the superficial weakest bridge with its matched melting threshold, and the integrity of the interfacial swapping bridges. Notably, genetic perturbation near the central lower gate simultaneously weakened both the superficial weakest and interfacial swapping bridges, accompanied by enhanced channel activity and a reduced heat-activation threshold. Taken together, these findings support the hypothesis that the superficial weakest bridges and interfacial swapping bridges are allosterically coupled during heat activation of hTRPV2 and that the C4-fold symmetry is essential for maintaining this coupling. Finally, the interplay between allosteric regulation by physical and chemical stimuli is discussed.

Results

A genetic perturbation near the central lower gate relocates the superficial weakest noncovalent bridge in asymmetric rTRPV2 $_{STD}$

When the segement ^{651}HVADN^{655} in rTRPV2 was replaced with the corrrsponding ^{651}SVATD^{655}of hTRPV2, the resulting rTRPV2$_{STD}$ mutant exhibited structural asymmetry (38). In the absence of phosphatidylethanolamine (PE) at the active vanilloid-binding site in the diagonal subunit B/D, thermoring analysis along the same PE-dependent minimal gating pathway from V254 to P726 revealed an increase in the total number of tertiary noncovalent bridges from 107 to 143, accompanied by a

decrease in the total number of grid sizes from 118 to 67 (Fig. 1A; Table S1). Consequently, the dynamic systematic thermal instability (T_i) decreased from 1.10 to 0.48 (Table 1) (32).

Table 1
Comparison of genetic perturbation-induced energetic and structural changes in the TRPV2 thermoring along the PE-dependent minimal gating pathway, spanning from V254-P726 in rTRPV2 or V253-P725 in hTRPV2. The comparative parameters are highlighted in bold.

Construct	**rTRPV2-$_{STD}$**	**rTRPV2-$_{STD}$**	**hTRPV2**	**hTRPV2-$_{HSN}$**
PDB ID	11ID	11ID	11HZ	11IA
Subunit	A/C	B/D	A/B/C/D	A/B/C/D
Lipid in the VSLD	PE	PE	CHL	CHL
Lipid at the active vanilloid site	PE	Free	PE	PE
Lipid environment	MSP2N2	MSP2N2	MSP2N2	MSP2N2
Sampling temperature, °C	4	4	4	4
Gating state	Inactivated	Inactivated	Inactivated	Inactivated
# of the biggest Grids	$Grid_4$	$Grid_5$	$Grid_8$	$Grid_7$
grid size (s)	4	5	8	7
The weakest bridge	Y471-PE-Q530	F407-I441	Q412-H436	Q412-H436
# of basic H-bonds (n) in stability equivalent to the weakest noncovalent bridge	2.0	1.3	2.3	1.8
Intensity of swapping bridge at the S4-S5 linker/S5' bridge (kcal/mol)	Broken Y525-R539'	Y525-R539' (1.4)	H519-R537'-Y523 (2–4)	H519-R537'-Y523 (1.5)
Total non-covalent interactions (N)	141	143	121	129
Total grid sizes (S), a.a	72	67	86	83
Systemic thermal instability (T_i)	**0.51**	**0.48**	**0.71**	**0.64**
Calculated $T_{m,th,}$ °C at E = 1 kcal/mol	**66**	**57**	**61**	**58**
Measured T_{th}, °C	**58**		**61**	**58**
Refs for T_{th}	**38**		**38**	**38**
Figures and legends				

Among these tertiary bridges, the weakest F407-I441 bridge was located in the voltage-sensor like domain (VSLD) and controlled by the biggest $Grid_5$ via a thermoring extending from F407 through F405, V409, Y412, H413, Q414, H438 and I441 before returning to F407 (Fig. 1B-C). Because this bridge had an energy equivalent to 1.3 basic H-bonds (1.3 kcal/mol), its calculated melting-temperature threshold ($T_{m,th}$) of 57°C closely matched the experimentally determined heat-activation threshold of 58°C (Table 1) (38). Notably, this weakest bridge differed from the weakest superficial bridges, K300-N354, S486-Y497 and L555-Y590, identified in close state 3 of native rTRPV2 (32). These findings indicate that the genetic perturbation near the central lower gate relocates the superficial weakest bridge associated with heat activation.

Notably, compared with the third closed state of native rTRPV2, the genetic perturbation near the central lower gate disrupted the interfacial swapping H521-R539', Y525-N639' and F612'-L594 π bridges in the absence of PE at the vanilloid-binding site. In contrast, the swapping Y412-R560', W509-F549', Y525-R539' and F618'-W496/P499 π interactions were preserved (Fig. 1D) (32).

In contrast, in the presence of PE at the vanilloid-binding site in the diagonal subunit A/C, thermoring analysis along the same PE-dependent minmal gating pathway revealed a slight decrease in the total number of tertiary noncovalent interactions from 143 to 141, accompanied by an increase in the total number of grid sizes from 67 to 72 (Fig. 2A, Table S2). Consequently, the dynamic systematic thermal instability (T_i) increased slightly from 0.48 to 0.51 (Table 1). Under this condition, the Y471-PE-Q530 bridge became the weakest and was governed by the biggest $Grid_4$ through a thermoring extending from Y471 through F472, Y514, Y515, R517, W660, H521, S526, Q530 and PE before returning to Y471 (Fig. 2B-C). Because the energy of this bridge was equivalent to that of 2 basic H-bonds (2 kcal/mol), its calculated melting-temperature threshold ($T_{m,th}$) was 66°C, deviating from the experimentally determined heat-activation threshold of 58°C (Table 1) (32).

More importantly, the presence of PE at the vanilloid-binding site disrupted not only the P499-F618' π bridge but also the Y525-R539' π bridge at the interface between the S4-S5 linker and S5' (Fig. 2D). Given that chemical perturbation of the swapping H521-R539'-Y525-N639' bridges near the central lower gate by 2-aminoethoxydiphenyl borate (2-APB) inactivates the rTRPV2 channel (39), these findings suggest that PE binding may further destabilize the interfacial swapping interactions, potentially resulting in partial inactivation of the asymmetric $rTRPV2_{STD}$ mutant channel.

A genetic perturbation near the central lower gate preserves the superficial weakest noncovalent bridge in symmetric $hTRPV2_{HDN}$

For the symmetric, native homotetrameric hTRPV2 channel, cholesterol (CHL) is located in each VSLD, whereas PE occupies the vanilloid-binding site (38). Along the same PE-dependent minimal gating pathway from V253 to P725, a total of 121 tertiary noncovalent bridges formed a systematic fluidic, grid-like mesh network comprising 86 grid sizes (Fig. 3A; Table S3). Accordingly, the dynamic systematic thermal instability (T_i) of 0.71 was higher than that of $rTRPV2_{STD}$ (Table 1).

Furthermore, the superficial weakest Q412-H436 bridge was located in the VSLD and governed by the biggest $Grid_8$ via a thermoring extending from Q477 through Q485, H436, Q412, H411, A407, T406, W507 and N509 before returning to Q477 (Fig. 3B-C). This bridge contained two H-bonds between Q412 and H436 and had an energetic equivalent of 2.3 basic H-bonds (2.3 kcal/mol). Accordingly, its calculated melting-temperature threshold ($T_{m,th}$) of 61°C exactly matched the experimentally determined heat-activation threshold of 61°C (Table 1) (38).

Because the K299-N352 bridge (corresponding to K300-N354 in rTRPV2) was absent, the native hTRPV2 channel was in an inactivated state (40). Compared with $rTRPV2_{STD}$, the hTRPV2 channel lacked the swapping Y410-Q558' bridge (corresponding to Y412-R560' in $rTRPV2_{STD}$) but exhibited an additional H519-R537' π bridge (corresponding to H521-R539' in $rTRPV2_{STD}$) near the PE lipid at the vanilloid-binding site (Fig. 3D). Accordingly, if the superficial weakest Q412-H436 bridge is allosterically coupled to the interfacial swapping H519-R537'-Y523 bridges near the central lower gate, a genetic perturbation in this swapping region would be expected to preserve the location of the superficial weakest bridge, although its melting-temperature threshold ($T_{m,th}$) could change.

To test this expectation, the three-dimensional cryo-EM structure of $hTRPV2_{HDN}$ was further analyzed. Following the repalcement of ^{651}SVATD^{655} with the corresponding ^{651}HVADN^{655} segment from rTRPV2 along the same PE-dependent minimal gating pathway from V253 to P725, the total numbers of tertiary noncovalent bridges and grid sizes changed from 121 and 86 to 129 and 83, respectively (Fig. 4A; Table S4). Consequently, the calculated dynamic systematic thermal instability (T_i) decreased from 0.71 to 0.64 (Table 1).

Most notably, the superfical Q412-H436 bridge in the VSLD remained the weakest but was then governed by the biggest $Grid_7$ via a thermoring extending from I439 through H436, Q412, T406, W507, M402 and Y401 before returning to I439 (Fig. 4B-C). Although the superficial Q412–H436 bridge contained only one H-bond, its energetic equivalent was 1.8 basic H-bonds (1.8 kcal/mol). Accordingly, its calculated melting-temperature threshold ($T_{m,th}$) of 58°C exactly matched the experimentally determined heat-activation threshold of 58°C (Table 1).

Furthermore, the CHL lipid remained anchored by Y476, Y512 and W676 (Fig. 4A), while the interfacial swapping bridges near the PE lipid were preserved, although the interfacial swapping H519-R537'-Y523 bridges were also weakened (Fig. 4D; Table 1). Notably, the simultaneous weakening of the weakest Q412–H436 bridge and the interfacial swapping bridges in in $hTRPV2_{HDN}$ was accompanied by a lower heat-activation threshold and enhanced heat-evoked activity (Table 1) (38). Collectively, these findings support the proposed allosteric coupling between the superficial weakest Q412–H436 bridge and the interfacial swapping H519-R537'-Y523 bridges near the central lower gate during heat activation of the hTRPV2 channel.

Discussion

Allosteric gating coupling has been extensively investigated in ligand-gated ion channels. In contrast, considerably less is known about the mechanisms of allosteric gating coupling in thermally gated ion channels. In this computational study, thermoring-mediated allosteric gating coupling was investigated in the thermosensitive TRPV2 channel. Notably, when compared with the ligand-activated CFTR channel, heat-evoked activation of TRPV2 also exhibited similar allosteric features, provided that the C4 symmetry was preserved.

Physical and chemical stimuli share similar allosteric regulatory mechanisms

Our previous studies demonstrated that genetic perturbations near the pseudosymmetry axis of two flexible transmembrane domains (TMDs) can allosterically regulate cystic fibrosis transmembrane conductance regulator (CFTR) channel activity in response to ATP and protein kinase A (PKA) (41–42). In the absence of such perturbations, the CFTR channel is stabilized in a closed state by the insertion of the regulatory (R) domain between TMD1 and TMD2, as well as between nucleotide binding domains 1 and 2 (NBD1 and NBD2) (43). PKA-mediated phosphorylation of the R domain releases this inhibitory constraint, thereby allowing the ATP-dependent dimerization of NBD1 and NBD2. This dimerization, in turn, allosterically strengthens the interaction between TMD1 and TMD2 and promotes the specific engagement of the dynamically phosphorylated S813 site with the TMD1/TMD2/NBD1 interfaces, collectively facilitating channel opening (44–46).

Alternatively, genetic perturbations, such as the K978C or P355A/S/F mutation at the base of transmembrane helix 9 or 6 (TM9 or TM6), respectively, located near the pseudosymmetry axis in the outer collar or pore region, can also strengthen the TMD1-TMD2 interaction (41–42, 45. This enhanced interaction facilitates R domain release and subsequent NBD1-NBD2 dimerization, ultimately promoting channel opening (47). Consequently, the K978C or P355A/S/F mutant exhibits greater sensitivity to ATP and PKA than the wild-type CFTR channel (41–42).

Similarly, the hTRPV2 channel is stabilized in a closed state at the physiological body temperature of 37°C by strong interfacial swapping H519-R537’-Y523 π bridges (Fig. 3D) (28, 29, 38, 48–52). When the temperature rises above the heat activation threshold of 61°C, thermal destabilization of the superficial weakest Q412-H438 bridge may disrupt the interfacial swapping bridges at the S4-S5 linker/S5’ interface, thereby promoting channel opening. However, when the residue swap at the TRP/S6 interface between hTRPV2 and rTRPV2 weakened the nearby interfacial swapping bridges, the superficial weakest Q412-H438 bridge was also allosterically destabilized. As a result, the $hTRPV2_{HDN}$ mutant can be activated at temperatures below 61°C, accompanied by enhanced heat-evoked channel activity (Fig. 5) (38).

Symmetry is essential for thermoring-driven allosteric gating coupling

CFTR is a monomeric protein with a pseudosymmetric topology between TMD1 and TMD2, as well as between NBD1 and NBD2 (43–44). Consequently, genetic mutations near the pseudosymmetry axis can allosterically regulate channel activity while preserving the ATP and PKA sites (46–47). In contrast, TRPV2 is a homotetrameric channel with C4-fold symmetry. This present study demonstrates that, when C4-fold symmetry is preserved in the $hTRPV2_{HDN}$ mutant, the superficial weakest Q412-H436 bridge remains in the same location and is associated with the interfacial swapping H519-R537'-Y523 bridges (Figs. 3–5). In contrast, the weakest bridge in the $rTRPV2_{STD}$ triple mutant is relocated following disruption of C4-fold symmetry (Figs. 1 & 2; Table 1). Taken together, these findings suggest that C4-fold symmetry is essential for maintaining the normal structural organization required for thermoring-driven allosteric gating coupling in TRPV2. Further studies involving similar genetic perturbations near the central lower gate are necessary to further examine the proposed allosteric coupling between the superficial weakest bridge and the interfacial swapping bridge at the S4-S5 linker/S5' interface in other thermosensitive TRP channels, including TRPV1, TRPV3, and TRPV4.

Interplay between allosteric regulation by physical and chemical stimuli

Gain-of-function (GOF) mutations have been extensively reported in ion channels, with some exhibiting constitutive activity in the absence of agonist, even at room temperature. Examples include the F640L mutation in rTRPV1 (53), as well as the R416Q/W, W521S, L655P, W692S/G, L694P, G568D/V/C, L673F and G573A/V/S/C Olmsted syndrome mutations in hTRPV3 (54–59). Given that the weakened interfacial swapping H519-R537'-Y523 bridges in $hTRPV2_{HDN}$ may also facilitate 2-APB binding, it is plausible that the mutant exhibits greater sensitivity to 2-APB than wild-type hTRPV2 (38).

In this context, constitutively active mutations as mentioned above in TRPV1 or TRPV3 may also alter temperature sensitivity. Further studies are needed to determine whether these mutations allosterically weakens both the interfacial swapping π bridges near the central lower gate and the superficial weakest tertiary bridges, thereby lowering the activation threshold and enhancing channel activity.

Conclusions

Allosteric mechanisms of protein activation by ligands have been extensively investigated. Although ligand binding shifts the equilibrium between inactive and active states, ligand-induced activation is not the only means of regulating protein function, as physical stimuli, such as temperature, can also drive protein activation above specific thermal thresholds. The thermosensitive hTRPV2 channel provides an illustrative example. Compared to rodent orthologs, wild-type hTRPV2 exhibits little or no activation below 61°C or in response to low concentrations of 2-APB at room temperature. However, a species-specific residue swap at the TRP/S6 interface between hTRPV2 and rTRPV2 renders the $hTRPV2_{HDN}$ mutant more sensitive to 2-APB and capable of heat activation at temperatures below 61°C but above 58°C.

The present computational study further reveals that allosteric gating coupling between the superficial weakest Q412-H436 bridges and the interfacial swapping H519-R537'-Y523 bridges near the central lower gate in the symmetric homotetrameric channel plays an important role in regulating hTRPV2 activity in response to both chemical (2-APB) and physical (heat) stimuli. Taken together, these findings provide a thermodynamic framework for understanding how structural symmetry and thermoring-mediated allosteric coupling contribute to the regulation of protein activity by chemical and physical stimuli.

Methods

Cryo-EM structures used

Three full-length, three-dimensional cryo-EM structures of apo TRPV2 channels in the inactivated state were analyzed to investigate the allosteric gating coupling between the superficial weakest tertiary noncovalent bridge and the interfacial swapping bridges near the central lower gate. These structures included rTRPV2$_{STD}$, wild type hTRPV2 and hTRPV2$_{HDN}$ (PDB IDs: 11ID, 11HZ and 11IA, with resolutions of 2.95 Å; 3.36 Å and 2.8 Å, respectively). The channels were purified in decyl maltose neopentyl glycol (DMNG) detergent and subsequently reconstituted in membrane scaffold protein 2N2 (MSP2N2) nanodiscs at pH 8 and 4°C (38).

Detecting and filtering tertiary noncovalent interactions

Along the same polypeptide chain, spanning residues from V254 to P726 in rTRPV2$_{STD}$ or from V253 to P725 in hTRPV2 and hTRPV2$_{HDN}$ (32, 38), pairs of tertiary noncovalent bridges were identified and sampled using UCSF Chimera according to the same stringent and consistent criteria established in previous studies (19–22, 32, 40, 46, 60–68). After excluding transient fluctuation-induced perturbations, the filtering parameters used to identify these tertiary bridges were applied consistently and detailed in the online Supporting Information (Tables S1–S4).

Mapping tertiary thermoring energetic structures using the grid thermodynamic model

In this study, the same simple yet highly sensitive energy network model as described in the previous studies was applied to investigate the thermoring-driven allosteric gating coupling in TRPV2. Briefly, when tertiary noncovalent interactions formed a systematic, fluidic, grid-like mesh network, the network can be mathematically constrained into thermoring structure within individual subunits using Graph theory and the Floyd–Warshall algorithm (69). Each thermoring resembled a DNA hairpin thermosensor and was characterized by a closed topological loop (70). Specifically, the loop began at one end of a

particular tertiary noncovalent bridge, followed the shortest path through adjacent polypeptide segments and/or other tertiary noncovalent bridges, and terminated at the opposite end of the same bridge.

The length of this shortest path, defined as the loop or grid size, was generally determined by the minimum number of free amino acid residues whose side chains do not involve tertiary noncovalent interactions. Because grid size influences the unfolding or melting temperature of each closed loop, or thermoring, this framework generates an energetic landscape that enables the local stability of individual thermorings to be evaluated and ranked according to their grid sizes, from biggest to smallest. Through this analysis, the weakest tertiary noncovalent bridge can be identified as a potential allosteric thermosensor that initiates global protein conformational changes when the temperature exceeds its corresponding melting-temperature threshold ($T_{m,th}$) (19–22, 32, 40, 46, 60–68).

Calculating the dynamic systematic thermal instability

The dynamic systematic thermal instability (T_i) was determined based on the following expression, as previously validated and tested in earlier studies (19–22, 32, 40, 46, 60–68):

$T_i = S/N$ (1)

where, *N* and *S* represent the total numbers of tertiary noncovalent interactions and grid sizes along the same polypeptide chain, respectively.

Calculating the melting temperature threshold for heat unfolding

The melting temperature threshold ($T_{m,th}$) for thermal unfolding of the least-stable noncovalent interaction within a specific grid at a physiological salt concentration of 150 mM NaCl was estimated using the following equation as previously described (19–22, 32, 40, 46, 60–68):

$T_{m,th}$ (°C) = 34 + (n − 2) × 10 + (20 − s) × 2 (2)

where, n represents the total number of basic H-bonds (approximately 1 kcal/mol each in a hydrophilic environment) that are energetically equivalent to the weakest noncovalent bridge governed by the corresponding grid, and s represents the size of the grid controlling the weakest tertiary bridge. According to this relationship, the static thermal stability of a grid increases either as the grid size decreases or as the number of energetically equivalent basic H-bonds increases.

Abbreviations

2-APB, 2-aminoethoxydiphenyl borate

CFTR, cystic fibrosis transmembrane conductance regulator

CHL, cholesterol

cryo-EM, cryo electron microscopy

DMNG, decyl maltose neopentyl glycol

GOF, Gain-of-function

MSP2N2, membrane scaffold protein 2N2

nucleotide binding domain (NBD)

PE, phosphatidylethanolamine

PC, phosphatidylcholine

PKA, protein kinase A

R, regulatory

T_i, systematic thermal instability

$T_{m,th}$, melting temperature threshold

TRP, transient receptor potential

TRPV, TRP vanilloid

TRPVi (i=1, 2, 3, 4)

TMD, transmembrane domain

TM, transmembrane helix

hTRPV2, human TRPV2

hTRPV3, human TRPV3

rTRPV2, rat TRPV2

VSLD, voltage-sensor-like domain

Declarations

Data availability

All data generated or analysed during this study are included in this published article and supplementary material.

Supporting information

This article contains supplementary material (Tables S1, S2, S3 and S4).

Funding Declaration

The work was supported by the NIDDK grant (2R56DK056796-10) and the American Heart Association (AHA) Grant (10SDG4120011 to GW).

Author contributions

G. W. wrote the main manuscript text and prepared Figures 1, 2, 3, 4, 5 and Table 1 and supplementary material (Tables S1, S2, S3 and S4), and reviewed the manuscript.

Competing interests

The author declares no conflict of interest.

References

1. Liu J, Nussinov R, Allostery (2016) An Overview of Its History, Concepts, Methods, and Applications. PLoS Comput Biol 12(6):e1004966. https://doi.org/10.1371/journal.pcbi.1004966
2. Wodak SJ, Paci E, Dokholyan NV, Berezovsky IN, Horovitz A, Li J, Hilser VJ, Bahar I, Karanicolas J, Stock G, Hamm P, Stote RH, Eberhardt J, Chebaro Y, Dejaegere A, Cecchini M, Changeux JP, Bolhuis PG, Vreede J, Faccioli P, Orioli S, Ravasio R, Yan L, Brito C, Wyart M, Gkeka P, Rivalta I, Palermo G, McCammon JA, Panecka-Hofman J, Wade RC, Di Pizio A, Niv MY, Nussinov R, Tsai CJ, Jang H, Padhorny D, Kozakov D, McLeish T (2019) Allostery in Its Many Disguises: From Theory to Applications. Structure 27(4):566–578. https://doi.org/10.1016/j.str.2019.01.003
3. Gunasekaran K, Ma B, Nussinov R (2004) Is allostery an intrinsic property of all dynamic proteins? Proteins 57(3):433–443. https://doi.org/10.1002/prot.20232
4. Kenakin T, Allostery (2024) The Good, the Bad, and the Ugly. J Pharmacol Exp Ther 388(1):110–120. https://doi.org/10.1124/jpet.123.001838
5. Raechell, Tee WV, Dong B, Guarnera E, Berezovsky IN (2026) On the Relationship Between Protein Stability, Thermostability, and Allosteric Signaling. J Mol Biol 438(4):169537. https://doi.org/10.1016/j.jmb.2025.169537
6. Tan ZW, Guarnera E, Tee WV, Berezovsky IN (2020) AlloSigMA 2: paving the way to designing allosteric effectors and to exploring allosteric effects of mutations. Nucleic Acids Res 48(W1). https://doi.org/10.1093/nar/gkaa338. ,W116-W124

7. Guarnera E, Berezovsky IN (2016) Structure-Based Statistical Mechanical Model Accounts for the Causality and Energetics of Allosteric Communication. PLoS Comput Biol 12(3):e1004678. https://doi.org/10.1371/journal.pcbi.1004678
8. Guarnera E, Berezovsky IN (2019) Toward Comprehensive Allosteric Control over Protein Activity. Structure 27(5):866–878. https://doi.org/10.1016/j.str.2019.01.014
9. Dong B, Tee WV, Berezovsky IN (2025) Designing Structure-specific and Switchable Allosteric Effectors for GPCRs Based on the Causality and Energetics of Inherent Signaling. J Mol Biol 437(20):169293. https://doi.org/10.1016/j.jmb.2025.169293
10. Tee WV, Tan ZW, Lee K, Guarnera E, Berezovsky IN (2021) Exploring the Allosteric Territory of Protein Function. J Phys Chem B 125(15):3763–3780. https://doi.org/10.1021/acs.jpcb.1c00540
11. Escobedo A, Voigt G, Faure AJ, Lehner B (2025) Genetics, energetics, and allostery in proteins with randomized cores and surfaces. Science 389(6758):eadq3948. https://doi.org/10.1126/science.adq3948
12. Weng C, Faure AJ, Escobedo A, Lehner B (2024) The energetic and allosteric landscape for KRAS inhibition. Nature 626(7999):643–652. https://doi.org/10.1038/s41586-023-06954-0
13. Saavedra HG, Wrabl JO, Anderson JA, Li J, Hilser VJ (2018) Dynamic allostery can drive cold adaptation in enzymes. Nature 558(7709):324–328. https://doi.org/10.1038/s41586-018-0183-2
14. Caterina MJ, Schumacher MA, Tominaga M, Rosen TA, Levine JD, Julius D (1997) The capsaicin receptor: a heat-activated ion channel in the pain pathway. Nature 389(6653):816–824. https://doi.org/10.1038/39807
15. Cao E (2020) Structural mechanisms of transient receptor potential ion channels. J Gen Physiol 152(3):e201811998. https://doi.org/10.1085/jgp.201811998
16. Teng J, Anishkin A, Kung C, Blount P (2019) Human mutations highlight an intersubunit cation-π bond that stabilizes the closed but not open or inactivated states of TRPV channels. Proc Natl Acad Sci U S A 116(19):9410–9416. https://doi.org/10.1073/pnas.1820673116
17. Kwon DH, Zhang F, Suo Y, Bouvette J, Borgnia MJ, Lee SY (2021) Heat-dependent opening of TRPV1 in the presence of capsaicin. Nat Struct Mol Biol 28(7):554–563. https://doi.org/10.1038/s41594-021-00616-3
18. Nadezhdin KD, Neuberger A, Trofimov YA, Krylov NA, Sinica V, Kupko N, Vlachova V, Zakharian E, Efremov RG, Sobolevsky AI (2021) Structural mechanism of heat-induced opening of a temperature-sensitive TRP channel. Nat Struct Mol Biol 28(7):564–572. https://doi.org/10.1038/s41594-021-00615-4
19. Wang G (2023) Thermoring-based heat activation switches in the TRPV1 biothermometer. Int J Biol Macromol 248:125915. https://doi.org/10.1016/j.ijbiomac.2023.125915
20. Wang G (2023) Thermoring basis for the TRPV3 bio-thermometer. *Sci Rep.* 13(1), 21594. https://doi:10.1038/s41598-023-47100-0. Erratum in: *Sci Rep.* 2024, 14(1), 4909. https://doi.org/10.1038/s41598-024-55395-w

21. Wang G (2025) Pathway-dependent cold activation of heat-responsive TRPV channels. Sci Rep 15(1):45041. https://doi.org/10.1038/s41598-025-29524-y
22. Wang G (2026) Temperature-dependent gating pathways in TRPV3. Sci Rep 16(1):15030. https://doi.org/10.1038/s41598-026-44194-0
23. Caterina MJ, Rosen TA, Tominaga M, Brake AJ, Julius D (1999) A capsaicin-receptor homologue with a high threshold for noxious heat. Nature 398:436–441. 10.1038/18906
24. Peier AM, Reeve AJ, Andersson DA, Moqrich A, Earley TJ, Hergarden AC, Story GM, Colley S, Hogenesch JB, McIntyre P, Bevan S, Patapoutian A (2002) A heat-sensitive TRP channel expressed in keratinocytes. Science 296(5575):2046–2049. https://doi.org/10.1126/science.1073140
25. Xu H, Ramsey IS, Kotecha SA, Moran MM, Chong JA, Lawson D, Ge P, Lilly J, Silos-Santiago I, Xie Y, DiStefano PS, Curtis R, Clapham DE (2002) TRPV3 is a calcium-permeable temperature-sensitive cation channel. Nature 418(6894):181–186. https://doi.org/10.1038/nature00882
26. Watanabe H, Vriens J, Suh SH, Benham CD, Droogmans G, Nilius B (2002) Heat-evoked activation of TRPV4 channels in a HEK293 cell expression system and in native mouse aorta endothelial cells. J Biol Chem 277(49):47044–47051. https://doi.org/10.1074/jbc.M208277200
27. Leffler A, Linte RM, Nau C, Reeh P, Babes A (2007) A high-threshold heat-activated channel in cultured rat dorsal root ganglion neurons resembles TRPV2 and is blocked by gadolinium. Eur J Neurosci 26:12–22. 10.1111/j.1460-9568.2007.05643.x
28. Neeper MP, Liu Y, Hutchinson TL, Wang Y, Flores CM, Qin N (2007) Activation properties of heterologously expressed mammalian TRPV2: evidence for species dependence. J Biol Chem 282(21):15894–15902. https://doi.org/10.1074/jbc.M608287200
29. Yao J, Liu B, Qin F (2011) Modular thermal sensors in temperature-gated transient receptor potential (TRP) channels. Proc Natl Acad Sci U S A 108:11109–11114. https://doi.org/10.1073/pnas.1105196108
30. Liu B, Qin F (2016) Use Dependence of Heat Sensitivity of Vanilloid Receptor TRPV2. Biophys J 110(7):1523–1537. https://doi.org/10.1016/j.bpj.2016.03.005
31. Mugo AN, Chou R, Qin F (2025) Protein dynamics underlies strong temperature dependence of heat receptors. Proc Natl Acad Sci U S A 122:e2406318121. https://doi.org/10.1073/pnas.2406318121
32. Wang G (2026) Thermodynamic coupling between cold and heat activations of TRPV2. Sci Rep 16(1):18024. https://doi.org/10.1038/s41598-026-54781-w
33. Liu B, Qin F (2021) Identification of a helix-turn-helix motif for high temperature dependence of vanilloid receptor TRPV2. J Physiol 599(21):4831–4844. https://doi.org/10.1113/JP282073
34. Haug FM, Pumroy RA, Sridhar A, Pantke S, Dimek F, Fricke TC, Hage A, Herzog C, Echtermeyer FG, de la Roche J, Koh A, Kotecha A, Howard RJ, Lindahl E, Moiseenkova-Bell V, Leffler A (2024) Functional and structural insights into activation of TRPV2 by weak acids. EMBO J 43(11):2264–2290. https://doi.org/10.1038/s44318-024-00106-4
35. Tee WV, Guarnera E, Berezovsky IN (2018) Reversing allosteric communication: From detecting allosteric sites to inducing and tuning targeted allosteric response. PLoS Comput Biol

14(6):e1006228. https://doi.org/10.1371/journal.pcbi.1006228

36. Lansky S, Betancourt JM, Zhang J, Jiang Y, Kim ED, Paknejad N, Nimigean CM, Yuan P, Scheuring S (2023) A pentameric TRPV3 channel with a dilated pore. Nature 621(7977):206–214. https://doi.org/10.1038/s41586-023-06470-1
37. Deng Z, Paknejad N, Maksaev G, Sala-Rabanal M, Nichols CG, Hite RK, Yuan P (2018) Cryo-EM and X-ray structures of TRPV4 reveal insight into ion permeation and gating mechanisms. Nat Struct Mol Biol 25(3):252–260. https://doi.org/10.1038/s41594-018-0037-5
38. Fricke TC, Pumroy RA, Rocereta JA, De Jesús-Pérez JJ, Oprita G, Meyer MJA, Herzog C, Echtermeyer FG, Hill K, Leffler A, Moiseenkova-Bell VY (2026) Structural origins of species-specific differences in TRPV2 activation. Nat Commun 17(1):8737. https://doi:10.1038/s41467-026-76831-7
39. Pumroy RA, Protopopova AD, Fricke TC, Lange IU, Haug FM, Nguyen PT, Gallo PN, Sousa BB, Bernardes GJL, Yarov-Yarovoy V, Leffler A, Moiseenkova-Bell VY (2022) Structural insights into TRPV2 activation by small molecules. Nat Commun 13(1):2334. https://doi.org/10.1038/s41467-022-30083-3
40. Wang G (2026) Inactivation switch for run-up in TRPV2. Reserach Square. https://doi.org/10.21203/rs.3.rs-9726674/v2
41. Wang W, Wu J, Bernard K, Li G, Wang G, Bevensee MO, Kirk KL (2010) ATP-independent CFTR channel gating and allosteric modulation by phosphorylation. Proc Natl Acad Sci U S A 107(8):3888–3893. https://doi:10.1073/pnas.0913001107
42. Wei S, Roessler BC, Chauvet S, Guo J, Hartman JL 4th, Kirk KL (2014) Conserved allosteric hot spots in the transmembrane domains of cystic fibrosis transmembrane conductance regulator (CFTR) channels and multidrug resistance protein (MRP) pumps. J Biol Chem 289(29):19942–19957. https://doi:10.1074/jbc.M114.562116
43. Liu F, Zhang Z, Csanády L, Gadsby DC, Chen J (2017) Molecular Structure of the Human CFTR Ion Channel. Cell 169(1):85–95e8. https://doi:10.1016/j.cell.2017.02.024
44. Fiedorczuk K, Iordanov I, Mihályi C, Szollosi A, Csanády L, Chen J (2024) The structures of protein kinase A in complex with CFTR: Mechanisms of phosphorylation and noncatalytic activation. Proc Natl Acad Sci U S A 121(46):e2409049121. https://doi:10.1073/pnas.2409049121
45. Wang W, Roessler BC, Kirk KL (2014) An electrostatic interaction at the tetrahelix bundle promotes phosphorylation-dependent cystic fibrosis transmembrane conductance regulator (CFTR) channel opening. J Biol Chem 289(44):30364–30378. https://doi:10.1074/jbc.M114.595710
46. Wang G (2025) Trikafta rescues F508del-CFTR by tightening specific phosphorylation-dependent interdomain interactions. Nat Sci 5:e70009. https://doi.org/10.1002/ntls.70009
47. Mihályi C, Töröcsik B, Csanády L (2016) Obligate coupling of CFTR pore opening to tight nucleotide-binding domain dimerization. Elife 5:e18164. https://doi:10.7554/eLife.18164
48. Boukalova S, Marsakova L, Teisinger J, Vlachova V (2010) Conserved residues within the putative S4-S5 region serve distinct functions among thermosensitive vanilloid transient receptor potential (TRPV) channels. J Biol Chem 285:41455–41462. https://doi:10.1074/jbc.M110.145466

49. Fricke TC, Echtermeyer F, Zielke J, de la Roche J, Filipovic MR, Claverol S, Herzog C, Tominaga M, Pumroy RA, Moiseenkova-Bell VY, Zygmunt PM, Leffler A, Eberhardt MJ (2019) Oxidation of methionine residues activates the high-threshold heat-sensitive ion channel TRPV2. Proc Natl Acad Sci U S A 116(48):24359–24365. https://doi.org/10.1073/pnas.1904332116
50. Mo X, Pang P, Wang Y, Jiang D, Zhang M, Li Y, Wang P, Geng Q, Xie C, Du HN, Zhong B, Li D, Yao J (2022) Tyrosine phosphorylation tunes chemical and thermal sensitivity of TRPV2 ion channel. Elife 11e78301. https://doi.org/10.7554/eLife.78301
51. Fricke TC, Rämisch A, Pumroy RA, Pantke S, Herzog C, Echtermeyer FG, Al-Samir S, Endeward V, Moiseenkova-Bell V, Leffler A (2025) Molecular determinants of 2-aminoethoxydiphenyl borate sensitivity of transient receptor potential vanilloid 2-unexpected differences between 2 rodent orthologs. Mol Pharmacol 107(8):100060. https://doi.org/10.1016/j.molpha.2025.100060
52. Kadkova A, Kadkova A, Kosinova K, Klouckova M, Strachotova D, Barvik I, Zimova L, Vlachova V (2026) TRPV2 and TRPC5 are potential targets for astringent phytochemicals. Curr Res Food Sci 12101306. https://doi:10.1016/j.crfs.2026.101306
53. Myers BR, Bohlen CJ, Julius D (2008) A yeast genetic screen reveals a critical role for the pore helix domain in TRP channel gating. Neuron 58(3):362–373. https://doi 10.1016/j.neuron.2008.04.012
54. Lin Z, Chen Q, Lee M, Cao X, Zhang J, Ma D, Chen L, Hu X, Wang H, Wang X, Zhang P, Liu X, Guan L, Tang Y, Yang H, Tu P, Bu D, Zhu X, Wang K, Li R, Yang Y (2012) Exome sequencing reveals mutations in TRPV3 as a cause of Olmsted syndrome. Am J Hum Genet 90(3):558–564. https://doi:10.1016/j.ajhg.2012.02.006
55. Cao X, Wang H, Li Y, Lee M, Jiang L, Zhou Y, Feng C, Lin Z, Yang Y (2016) Semidominant Inheritance in Olmsted Syndrome. J Investig Dermatol 136:1722–1725. https://doi:10.1016/j.jid.2016.04.024
56. Zhong W, Hu L, Cao X, Zhao J, Zhang X, Lee M, Wang H, Zhang J, Chen Q, Feng C, Duo L, Wang X, Tang L, Lin Z, Yang Y (2021) Genotype–Phenotype Correlation of TRPV3-Related Olmsted Syndrome. J Invest Dermatol 141(3):545–554. https://doi:10.1016/j.jid.2020.06.035
57. Jain A, Sahu RP, Goswami C (2022) Olmsted syndrome causing point mutants of TRPV3 (G568C and G568D) show defects in intracellular Ca^{2+}-mobilization and induce lysosomal defects. Biochem Biophys Res Commun 628:32–39. https://doi:10.1016/j.bbrc.2022.08.026
58. Mo R, Ma X, Hu L, Tan Y, Qiang L, Yang Y, Wang X, Chen Z (2024) The cumulative effect of compound heterozygous variants in TRPV3 caused Olmsted syndrome. J Dermatol Sci 116:111–119. https://doi:10.1016/j.jdermsci.2024.11.003
59. Khau J, Purohit R, Nadezhdin KD, Talyzina IA, Sobolevsky AI (2026) Structural diversity of heat-sensing channel TRPV3 with Olmsted syndrome mutations. Nat Commun 17(1):7793. https://doi:10.1038/s41467-026-74687-5
60. Wang G (2023) The network basis for the structural thermostability and the functional thermoactivity of aldolase B. Molecules 28:1850. https://doi:10.3390/molecules28041850
61. Wang G (2023) Network basis for the heat-adapted structural thermostability of bacterial class II fructose bisphosphate aldolase. ACS Omega 8:17731–17739.

https://doi.org/10.1021/acsomega.3c00473

62. Wang G (2023) Thermal ring-based heat switches in hyperthermophilic class II bacterial fructose aldolase. ACS Omega 8:24624–24634. https://doi.org/10.1021/acsomega.3c03001
63. Wang G (2024) Phosphatidylinositol-4,5-biphosphate (PIP_2)-Dependent Thermoring Basis for Cold-Sensing of the Transient Receptor Potential Melastatin-8 (TRPM8) Biothermometer. Physchem 4:106–119. https://doi.org/10.3390/physchem4020008
64. Wang G (2024) Thermoring basis for heat unfolding-induced inactivation in TRPV1. Nat Sci 4:e20240008. https://doi.org/10.1002/ntls.20240008
65. Wang G (2025) ATP-dependent thermoring basis for the heat unfolding of the first nucleotide-binding domain isolated from human CFTR. Nat Sci 5:e70007. https://doi.org/10.1002/ntls.70007
66. Wang G (2025) Thermodynamic coupling between folding correctors and the first of dimerized nucleotide binding domains in CFTR. ACS Bio Med Chem Au 5:593–601. https://doi.org/10.1021/acsbiomedchemau.5c00014
67. Wang G (2026) Trikafta restores thermodynamic coupling between two nucleotide binding domains for potentiating CFTR activity. Biomed Pharmacother 194:118936. https://doi.org/10.1016/j.biopha.2025.118936
68. Wang G (2026) Thermoring basis for the proton-driven heat activation of a cation-selective channel in myriapods. *Sci. Rep.* 16, 1949. https://doi.org/10.1038/s41598-025-31732-5
69. Floyd RW (1962) Algorithm-97 - *Shortest Path*. Commun Acm 5:345–345
70. Jonstrup AT, Fredsøe J, Andersen AH (2013) DNA hairpins as temperature switches, thermometers and ionic detectors. Sensors 13:5937–5944. https://doi:10.3390/s130505937

Figures

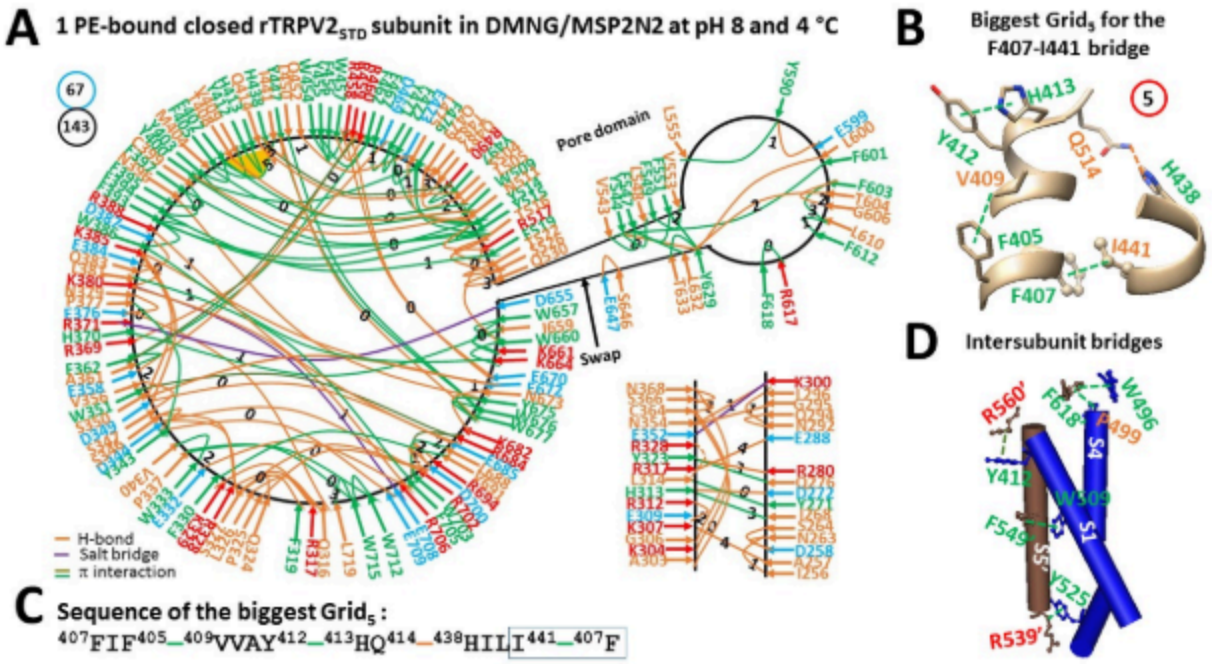


Figure 1

Thermoring structures of 1-PE bound closed rTRPV2$_{STD}$ subunit at low temperature.

(**A)** Grid-like mesh network of noncovalent interactions along the PE-dependent minimal gating pathway within a single subunit B/D of 1-PE-bound closed rTRPV2$_{STD}$ reconstituted in a DMNG/MSP2N2 nanodisc at pH 8 and 4 °C (PDB: 11ID). The same color scheme for residues and arrows is used throughout for ease of identification. Salt bridges, p interactions, and H-bonds between paired amino acid side chains along the PE-dependent minimal gating pathway from V254 to P726 are represented by purple, green, and orange lines, respectively. The specific constrained grid sizes necessary to regulate the least-stable noncovalent interactions within each grid are indicated with black numbers. The identified least-stable F407-I441 bridge within the biggest Grid$_5$ is highlighted in orange. The total grid sizes and the total number of grid size-controlled noncovalent interactions along the PE-dependent minimal gating pathway are indicated in cyan and black circles, respectively. (**B)** Structure of the biggest Grid$_5$ with a 5-residue size to regulate the weakest F407-I441 bridge in the VSLD. (**C)** Amino acid sequence of the biggest Grid$_5$ to control the weakest F407-I441 bridge highlighted in the blue box. (**D**) Swapped interactions at the VSLD/PD'/S4-S5 linker interfaces near the PE binding site and upper and lower gates in the 1-PE bound closed state.

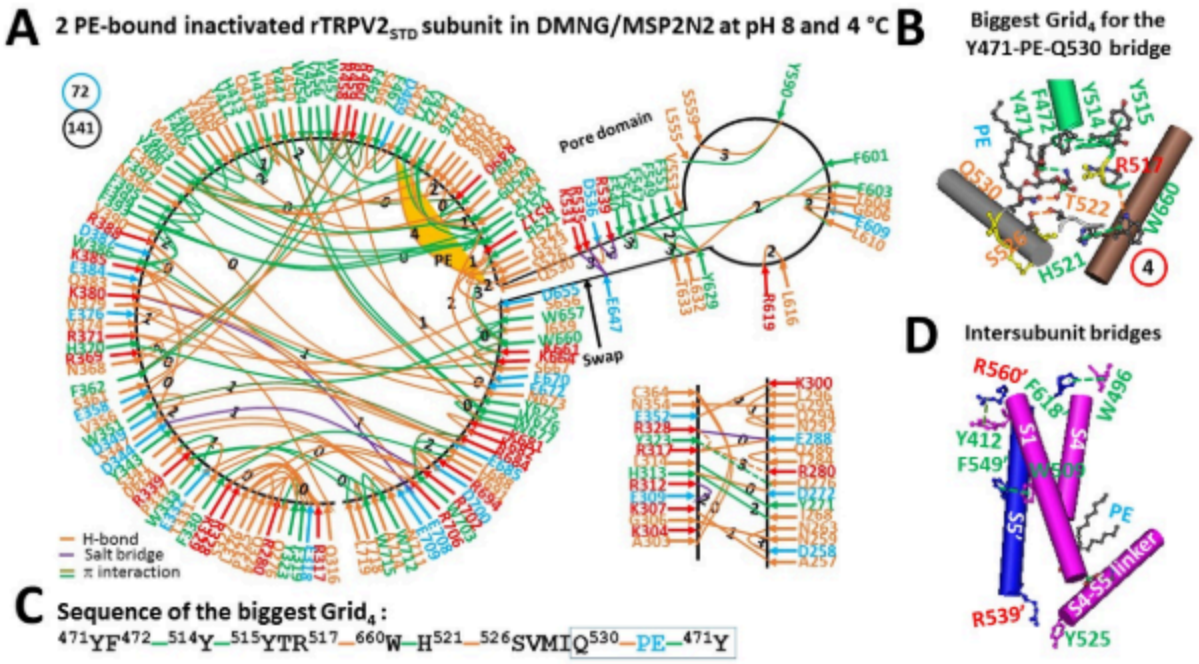


Figure 2

Thermoring structures of 2-PE bound inactivated rTRPV2$_{STD}$ subunit at low temperature.

(**A)** Grid-like mesh network of noncovalent interactions along the PE-dependent minimal gating pathway within a single subunit A/C of 2-PE-bound inactivated rTRPV2$_{STD}$ reconstituted in a DMNG/MSP2N2 nanodisc at pH 8 and 4 °C (PDB: 11ID). The same color scheme for residues and arrows is used throughout for ease of identification. Salt bridges, p interactions, and H-bonds between paired amino acid side chains along the PE-dependent minimal gating pathway from V254 to P726 are represented by purple, green, and orange lines, respectively. The specific constrained grid sizes necessary to regulate the least-stable noncovalent interactions within each grid are indicated with black numbers. The identified least-stable Y471-PE-Q530 bridge within the biggest Grid$_4$ is highlighted in orange. The total grid sizes and the total number of grid size-controlled noncovalent interactions along the PE-dependent minimal gating pathway are indicated in cyan and black circles, respectively. (**B)** Structure of the biggest Grid$_4$ with a 4-residue size to regulate the weakest Y471-PE-Q530 bridge at the internal S4/S4-S5 linker interface. (**C)** Amino acid sequence of the biggest Grid$_4$ to control the weakest Y471-PE-Q530 bridge highlighted in the blue box. (**D**) Swapped interactions at the VSLD/PD'/S4-S5 linker interfaces near the PE binding site and upper and lower gates in the 2-PE bound closed state.

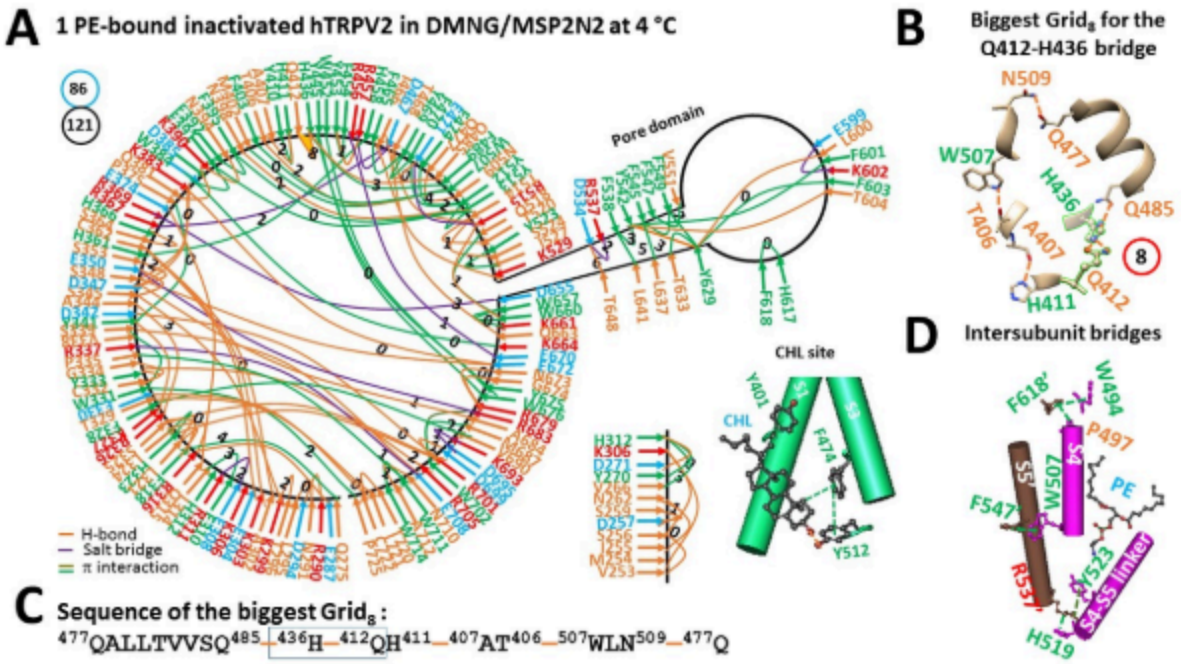


Figure 3

Thermoring structures of 1-PE bound inactivated hTRPV2 at low temperature.

(**A)** Grid-like mesh network of noncovalent interactions along the PE-dependent minimal gating pathway within a single subunit of 1-PE-bound inactivated hTRPV2 reconstituted in a DMNG/MSP2N2 nanodisc at pH 8 and 4 °C (PDB: 11HZ). The same color scheme for residues and arrows is used throughout for ease of identification. Salt bridges, p interactions, and H-bonds between paired amino acid side chains along the PE-dependent minimal gating pathway from V253 to P725 are represented by purple, green, and orange lines, respectively. The specific constrained grid sizes necessary to regulate the least-stable noncovalent interactions within each grid are indicated with black numbers. The identified least-stable Q412-H436 bridge within the biggest $Grid_8$ is highlighted in orange. The total grid sizes and the total number of grid size-controlled noncovalent interactions along the PE-dependent minimal gating pathway are indicated in cyan and black circles, respectively. The inset is the CHL binding site. (**B)** Structure of the biggest $Grid_8$ with an 8-residue size to regulate the weakest Q412-H436 bridge in the VSLD. (**C)** Amino acid sequence of the biggest $Grid_8$ to control the weakest Q412-H436 bridge highlighted in the blue box. (**D**) Swapped interactions at the VSLD/PD'/S4-S5 linker interfaces near the PE binding site and upper and lower gates in the 1-PE bound inactivated state.

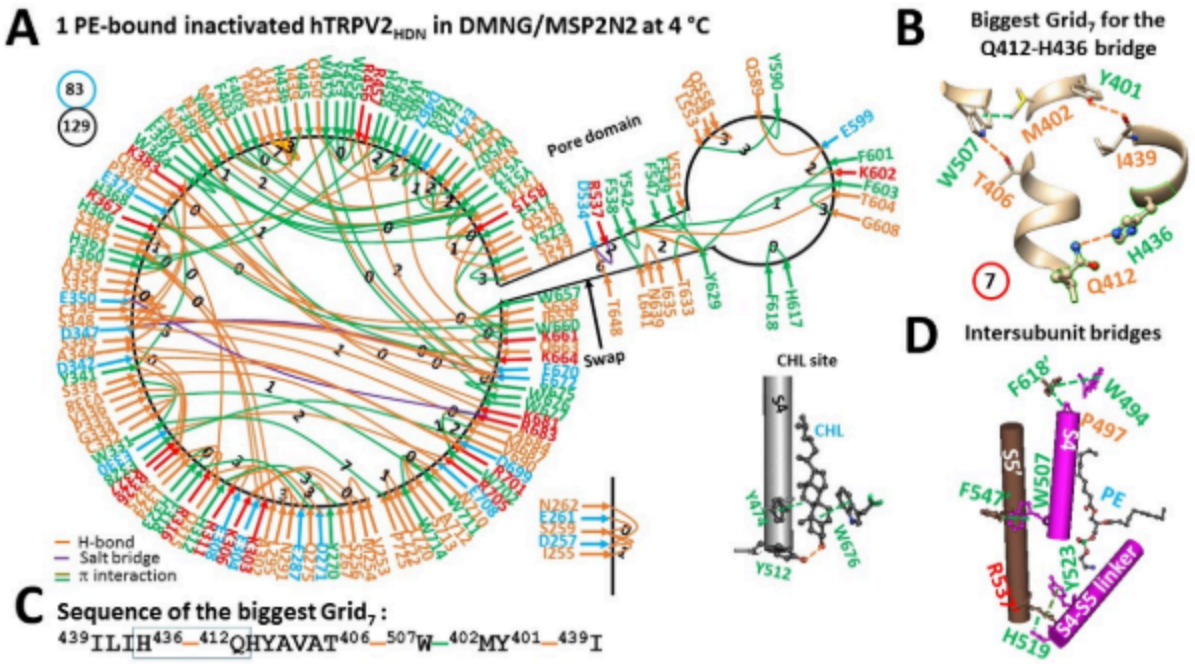


Figure 4

Thermoring structures of 1-PE bound inactivated hTRPV2$_{HDN}$ at low temperature.

(**A)** Grid-like mesh network of noncovalent interactions along the PE-dependent minimal gating pathway within a single subunit of 1-PE-bound inactivated hTRPV2$_{HDN}$ reconstituted in a DMNG/MSP2N2 nanodisc at pH 8 and 4 °C (PDB: 11IA). The same color scheme for residues and arrows is used throughout for ease of identification. Salt bridges, p interactions, and H-bonds between paired amino acid side chains along the PE-dependent minimal gating pathway from V253 to P725 are represented by purple, green, and orange lines, respectively. The specific constrained grid sizes necessary to regulate the least-stable noncovalent interactions within each grid are indicated with black numbers. The identified least-stable Q412-H436 bridge within the biggest Grid$_7$ is highlighted in orange. The total grid sizes and the total number of grid size-controlled noncovalent interactions along the PE-dependent minimal gating pathway are indicated in cyan and black circles, respectively. The inset is the CHL binding site. (**B)** Structure of the biggest Grid$_7$ with a 7-residue size to regulate the weakest Q412-H436 bridge in the VSLD. (**C)** Amino acid sequence of the biggest Grid$_7$ to control the weakest Q412-H436 bridge highlighted in the blue box. (**D**) Swapped interactions at the VSLD/PD'/S4-S5 linker interfaces near the PE binding site and upper and lower gates in the 1-PE bound inactivated state.**Thermoring structures of 1-PE bound inactivated hTRPV2$_{HDN}$ at low temperature.**

(**A)** Grid-like mesh network of noncovalent interactions along the PE-dependent minimal gating pathway within a single subunit of 1-PE-bound inactivated hTRPV2$_{HDN}$ reconstituted in a DMNG/MSP2N2 nanodisc at pH 8 and 4 °C (PDB: 11IA). The same color scheme for residues and arrows is used throughout for ease of identification. Salt bridges, p interactions, and H-bonds between paired amino acid side chains along the PE-dependent minimal gating pathway from V253 to P725 are represented by

purple, green, and orange lines, respectively. The specific constrained grid sizes necessary to regulate the least-stable noncovalent interactions within each grid are indicated with black numbers. The identified least-stable Q412-H436 bridge within the biggest $Grid_7$ is highlighted in orange. The total grid sizes and the total number of grid size-controlled noncovalent interactions along the PE-dependent minimal gating pathway are indicated in cyan and black circles, respectively. The inset is the CHL binding site. (**B)** Structure of the biggest $Grid_7$ with a 7-residue size to regulate the weakest Q412-H436 bridge in the VSLD. (**C)** Amino acid sequence of the biggest $Grid_7$ to control the weakest Q412-H436 bridge highlighted in the blue box. (**D**) Swapped interactions at the VSLD/PD'/S4-S5 linker interfaces near the PE binding site and upper and lower gates in the 1-PE bound inactivated state.

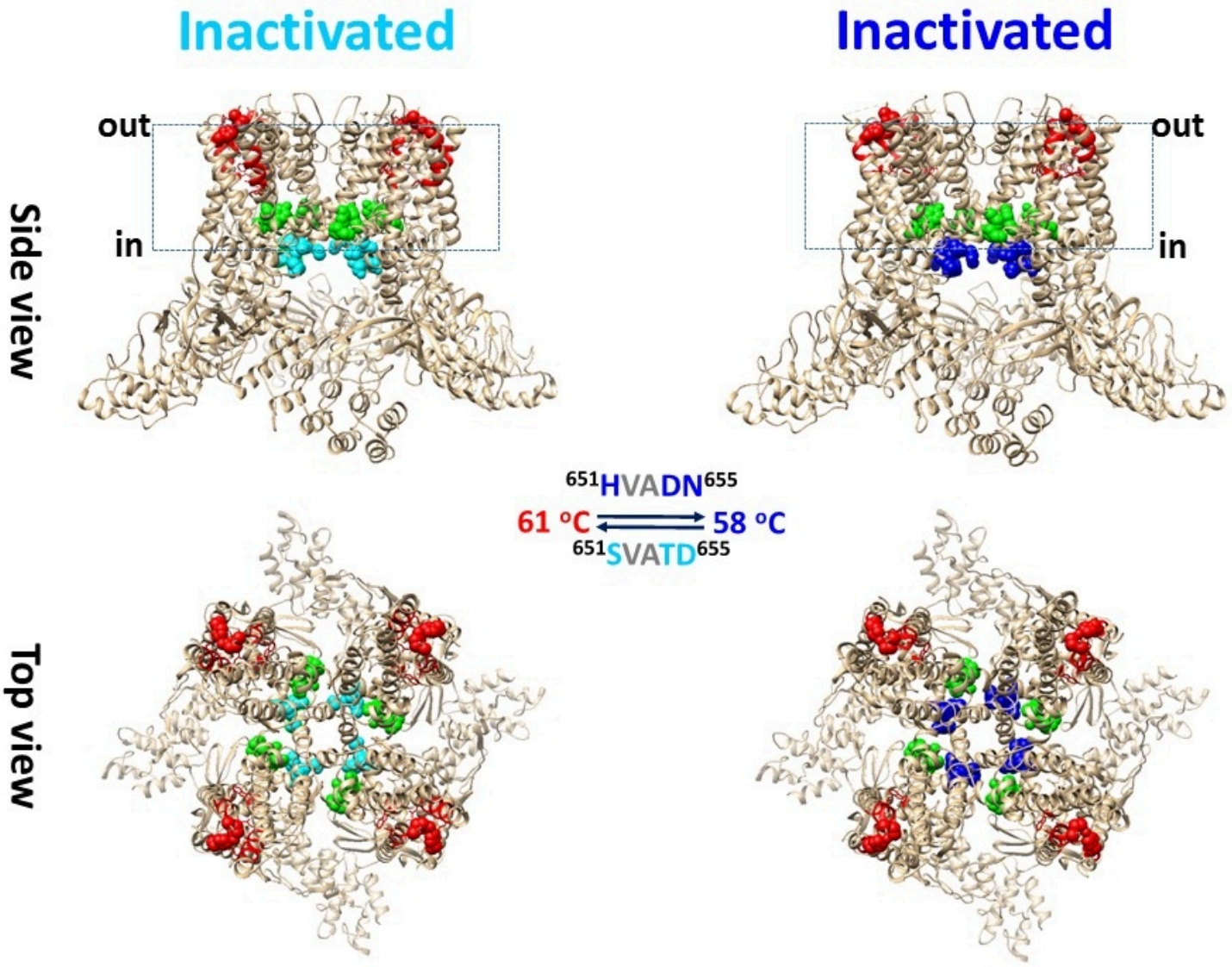


Figure 5

Working model of thermoring-driven allosteric gating coupling of hTRPV2. The homo-tetrameric cryo-EM structures of hTRPV2 and $hTRPV2_{HDN}$ in PE-bound, inactivated states at pH 8 and 4 °C (PDB ID, 11HZ and 11IA, respectively) were utilized to develop the model. Despite genetic perturbation near the central

lower gate (cyan), the biggest thermoring exhibits only minor structural and size changes. However, the allosteric gating coupling between the superficial, weakest Q412-H436 bridges (red) in the VSLD and the interfacial, domain-swapped H521-R539’ bridges (green) near the central lower gate is maintained, together with the C4 symmetry.

Supplementary Files

This is a list of supplementary files associated with this preprint. Click to download.

- SupplementarymaterialthermoringdrivengatingcouplinginTRPV2v1.0.pdf